Parametric Raman crystalline anti-Stokes laser at 503 nm with collinear beam interaction at tangential phase matching

S. N. Smetanin[1,2] · M. Jelínek[3] · V. Kubeček[3]

Abstract Stimulated-Raman-scattering in crystals can be used for the single-pass frequency-conversion to the Stokes-shifted wavelengths. The anti-Stokes shift can also be achieved but the phase-matching condition has to be fulfilled because of the parametric four-wave mixing process. To widen the angular-tolerance of four-wave mixing and to obtain high-conversion-efficiency into the anti-Stokes, we developed a new scheme of the parametric Raman anti-Stokes laser at 503 nm with phase-matched collinear beam interaction of orthogonally-polarized Raman components in calcite oriented at the phase-matched angle under 532 nm 20 ps laser excitation. The excitation laser beam was split into two orthogonally-polarized components entering the calcite at the certain incidence angles to fulfill the nearly collinear phase-matching and also to compensate walk-off of extraordinary waves for collinear beam interaction. The phase matching of parametric Raman interaction is tangential and insensitive to the angular mismatch if the Poynting vectors of the biharmonic pump and parametrically generated (anti-Stokes) waves are collinear. For the first time it allows to achieve experimentally the highest conversion efficiency into the anti-Stokes wave (503 nm) up to 30% from the probe wave and up to 3.5% from both pump and probe waves in the single-pass picosecond parametric calcite Raman laser. The highest anti-Stokes pulse energy was 1.4 μJ.

1 Introduction

Stimulated Raman scattering (SRS) in crystals can be used as a simple and non-expensive solution for the single-pass frequency conversion to the Stokes-shifted wavelengths that are not readily available from solid-state lasers. Anti-Stokes shift of the laser frequency can also be realized using Raman-active media but the phase matching has to be fulfilled because it is a parametric four-wave mixing (FWM) process at resonant Raman nonlinearity where two photons of the fundamental laser radiation interacting with one Stokes photon produce one anti-Stokes photon. Therefore the parametric Raman anti-Stokes laser requires not only phase matching, but also biharmonic pumping by two waves having frequency difference equal to the Raman frequency of the Raman-active medium. The anti-Stokes FWM generation under pumping by both the fundamental laser wave and the separately-generated Stokes wave propagating at the required phase matched angles has been demonstrated in high pressure hydrogen [1, 2] and in a KGd(WO$_4$)$_2$ crystal [3]. The simplest approach to the problem of a phase-matched parametric Raman anti-Stokes laser is to generate not only an anti-Stokes wave (by FWM) but also a Stokes wave (by SRS) in single Raman-active medium. Phase-matched conical anti-Stokes self-conversion at SRS is well-known [4] but anti-Stokes cones cannot be applied in most cases. A phase-matched parametric Raman anti-Stokes laser generating low divergence collimated anti-Stokes output under extracavity pumping by a single laser

✉ S. N. Smetanin
ssmetanin@bk.ru

M. Jelínek
michal.jelinek@fjfi.cvut.cz

1   A.M. Prokhorov General Physics Institute, Russian Academy of Sciences, Vavilova 38, Moscow, Russian Federation

2   National University of Science and Technology MISiS, Leninski Prospekt 4, Moscow, Russian Federation

3   Czech Technical University in Prague, Faculty of Nuclear Sciences and Physical Engineering, Břehová 7, Prague, Czech Republic

beam tilted at the phase-matched angle was proposed and realized for the first time in 1990 [5] using high pressure hydrogen as Raman-active medium. Similar crystalline parametric Raman anti-Stokes lasers were realized later using KGd (WO$_4$)$_2$ [6] and BaWO$_4$ [7] Raman crystals. However, a vast majority of the known parametric Raman anti-Stokes lasers have very low conversion efficiencies of about 1% at theoretically predicted values of up to 40% [1]. It can be explained by that these lasers are based on non-collinear phase matching of parametric Raman interaction for compensation of dispersion wave mismatch, but the non-collinear phase matching has a short effective interaction length and narrow angular tolerance in comparison with the angular divergence of the interacting beams.

To increase the efficiency of the parametric Raman lasers the possibilities of phase matching for collinear four-wave-mixing interaction can be used. A collinear phase-matched FWM interaction of orthogonally polarized SRS components was proposed in [8]. In the experimental setup [8] based on a long Raman-active CaCO$_3$ crystal two input waves with different frequencies (a pump ordinary wave for SRS and a probe extraordinary wave for FWM) tilted at the certain angles not only to fulfill phase matching but also to increase the effective interaction length were used. In [9] using a short CaCO$_3$ crystal rotated inside the optical cavity allowed to realize the phase-matched FWM interaction of orthogonally polarized SRS components using only one (pump) input 532-nm wave directed along the cavity axis, but the parametric Raman conversion efficiency was low because of the walk-off effect which was only decreased but not fully compensated. Using a 90°-angle phase matching in the a-cut Nd:SrMoO$_4$ crystal allowed to prevent the walk-off effect and to realize the collinear self-Raman parametric generation under longitudinal laser-diode pumping [10] but the parametric Raman conversion efficiency was low again (~1%) because the orthogonally polarized components were not specially generated and took place only due to 10-% depolarization.

In our present investigation, to obtain high conversion efficiency into the anti-Stokes wave we propose and study a new scheme of the parametric Raman anti-Stokes laser at 503 nm with phase-matched collinear beam interaction of orthogonally polarized Raman components in calcite under 20 ps laser pumping at 532 nm. We use only one 532 nm laser source to excite the Raman-active calcite crystal oriented at the phase matched angle for orthogonally polarized Raman components four-wave mixing. Additionally, we split the 532 nm laser radiation into the orthogonally polarized components (a pump ordinary wave and a probe extraordinary wave) entering into the Raman-active calcite crystal at the certain incidence angles to fulfill the nearly collinear phase matching and also to compensate walk-off of extraordinary waves for collinear beam interaction in the crystal with the widest angular tolerance of FWM.

2 Theoretical study of angular tolerance of parametric Raman interaction phase matching in crystals

As it is known from the works [1–3, 5–7] the main problem of the parametric Raman anti-Stokes lasers is low conversion efficiency that is explained by too high angular divergence of the interacting beams leading to the wave mismatch of Stokes-anti-Stokes coupling in spite of maintaining the phase-matched conditions. To solve this problem we need to analyze the angular dependence of wave mismatch and determine the phase matching angular tolerance in dependence on the Raman-active medium parameters.

Figure 1 shows a diagram of FWM interaction angular mismatch of wave vectors of the laser pump ($\mathbf{k}_L$), Stokes ($\mathbf{k}_S$), and anti-Stokes ($\mathbf{k}_A$) radiation in the Raman-active medium. Phase matching takes place at the angle of $\Delta\Theta_{PM}$ between the pump and Stokes wave vectors. Angular mismatch leads to appearance of wave mismatch vector $\Delta\mathbf{k}$ collinear to the anti-Stokes wave vector because the anti-Stokes wave emerges at an angle that minimizes the wave mismatch [1].

Using the diagram in Fig. 1 the angular dependence of an absolute value of the wave mismatch Δk is determined as [1]

$$\Delta k(\Delta\Theta) = k_A - \sqrt{(2k_L - k_S \cos\Delta\Theta)^2 + (k_S \sin\Delta\Theta)^2}, \tag{1}$$

where k_L, k_S and k_A are absolute values of wave vectors of the pump, Stokes, and anti-Stokes radiation respectively; $\Delta\Theta$ is the angle between the laser pump and Stokes wave vectors. The phase-matched angle $\Delta\Theta_{PM}$ corresponding to the phase matching condition ($\Delta k = 0$) is non-zero because of the medium dispersion. Then, at $\Delta\Theta = 0$ we have collinear wave mismatch according to [11]:

$$\begin{aligned}\Delta k_0 &= k_S + k_A - 2k_L \\ &= (n_S + n_A - 2n_L)\, 2\pi\, \lambda_L^{-1} + (n_A - n_S)\, 2\pi\, \nu_R,\end{aligned} \tag{2}$$

where n_L, n_S, and n_A are refractive indices for the pump, Stokes, and anti-Stokes waves respectively;
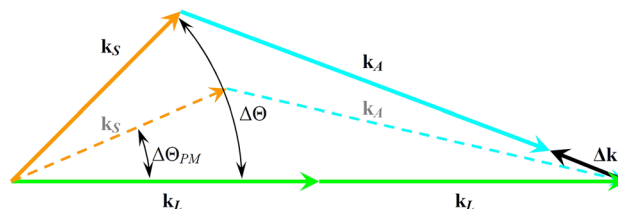

Fig. 1 A diagram of angular mismatch of FWM interaction of wave vectors of the laser pump ($\mathbf{k}_L$), Stokes ($\mathbf{k}_S$) and anti-Stokes ($\mathbf{k}_A$) radiation

$k_{L,S,A} = n_{L,S,A} \, 2\pi/\lambda_{L,S,A}$; λ_L is the laser pump wavelength; $\lambda_{S,A} = (\lambda_L^{-1} \mp \nu_R)^{-1}$ are the Stokes and anti-Stokes wavelengths; ν_R is the Raman frequency (in cm^{-1}) of the medium.

Usually the phase-matched angle $\Delta\Theta_{PM}$ is low and we can expand the expression (1) to Taylor series and obtain the approximate expression:

$$\Delta k(\Delta\Theta) \approx \Delta k_0 - \frac{k_L k_S}{k_A} \Delta\Theta^2. \tag{3}$$

The expression (3) is valid when $\Delta\Theta < 100$ mrad which takes place practically in all cases. Thus the wave mismatch is proportional to the squared angle between the pump and Stokes beams in the medium. So, we have phase matching ($\Delta k = 0$) at

$$\Delta\Theta_{PM} = \pm\sqrt{\frac{\Delta k_0}{k_L k_S/k_A}}. \tag{4}$$

The phase matching will be completely lost during one pass for $\Delta k = \pm\pi/L$, where L is the Raman-active medium length [6]. From the point of (3) it corresponds to the critical values of positive and negative angular mismatches (from $\Delta\Theta_{PM}$)

$$\delta\Theta_{PM}^{(+)} = \sqrt{\frac{\Delta k_0 + \pi/L}{k_L k_S/k_A}} - \Delta\Theta_{PM}, \tag{5}$$

$$\delta\Theta_{PM}^{(-)} = \Delta\Theta_{PM} \pm \sqrt{\frac{\Delta k_0 \pm \pi/L}{k_L k_S/k_A}}, \tag{6}$$

and the angular tolerance of phase matching is the sum of (5) and (6), i.e.

$$\delta\Theta_{PM} = \sqrt{\frac{\Delta k_0 + \pi/L}{k_L k_S/k_A}} \pm \sqrt{\frac{\Delta k_0 \pm \pi/L}{k_L k_S/k_A}}, \tag{7}$$

where the sign "+" is for $\Delta k_0 \leq \pi/L$ and the sign "–" is for $\Delta k_0 > \pi/L$.

As it follows from (7) at $\Delta k_0 \leq \pi/L$ the angular tolerance $\delta\Theta_{PM}$ is the widest:

$$\delta\Theta_0 = 2\sqrt{\frac{\Delta k_0 + \pi/L}{k_L k_S/k_A}}, \tag{8}$$

that is centered relative to the zero angle $\Delta\Theta = 0$, both (positive and negative) phase-matched angles $\Delta\Theta_{PM}$ (4) are inside the angular tolerance $\delta\Theta_0$, i.e. such four-wave mixing insensitive to the angular mismatch is collinear. Therefore the range $\Delta k_0 \leq \pi/L$ can be accepted as the condition for collinear four-wave mixing insensitive to the angular mismatch. However having high collinear

wave mismatch Δk_0 this condition can be fulfilled only at significant shortening of Raman active medium leading to increasing the SRS threshold limited by the medium optical damage threshold.

At $\Delta k_0 > \pi/L$ we have a decreased value of the angular tolerance inversely proportional to $\Delta k_0 L$:

$$\delta\Theta_{PM} = \sqrt{\frac{\Delta k_0 + \pi/L}{k_L k_S/k_A}} - \sqrt{\frac{\Delta k_0 - \pi/L}{k_L k_S/k_A}} \approx \frac{\pi \, |\Delta\Theta_{PM}|}{\Delta k_0 L}, \tag{9}$$

that is approximately centered relative to the phase-matched angle $\Delta\Theta_{PM}$.

Let's estimate the angular tolerance for the known crystalline parametric Raman anti-Stokes lasers based on a KGd(WO$_4$)$_2$ crystal ($\nu_R = 901$ cm^{-1} and $\nu_R = 768$ cm^{-1}) [3, 6] pumped by a 0.532-μm Nd:YAG laser second harmonics. Using the refractive index data of a KGd(WO$_4$)$_2$ crystal [12], from (2) and (4) for the Raman frequency of $\nu_R = 901$ cm^{-1} we get $\Delta k_0 \approx 145.5$ cm^{-1} and $\Delta\Theta_{PM} \approx 25.7$ mrad, and for the Raman frequency of $\nu_R = 768$ cm^{-1} we obtain $\Delta k_0 \approx 113.5$ cm^{-1} and $\Delta\Theta_{PM} \approx 22.2$ mrad. In the work [6] the KGd(WO$_4$)$_2$ crystal with $\nu_R = 901$ cm^{-1} and $L = 2.5$ cm was used, and so Δk_0 exceeded π/L by 116 times, then $\delta\Theta_{PM} \approx \pi \, |\Delta\Theta_{PM}|/\Delta k_0 L \approx 0.22$ mrad that is essentially lower than the Stokes beam divergence (6.4 mrad) leading to very low conversion efficiency of about 0.5% [6]. In the work [3] the KGd(WO$_4$)$_2$ crystal with lower values of $L = 1$ cm and $\nu_R = 768$ cm^{-1} was used, and so Δk_0 exceeded π/L by 36 times, then from (9) we get $\delta\Theta_{PM} \approx 0.62$ mrad that is 3 times wider than in the previous case leading to higher conversion efficiency to the anti-Stokes wave of about 4% (it is calculated from one wave of biharmonic pumping, and so the overall optical efficiency was lower).

Thus, low efficiency of the known crystalline parametric Raman lasers can be explained by too high angular divergence of the interacting beams in comparison with phase matching angular tolerance. However it is possible to get phase matching insensitive to the angular mismatch if the interaction is collinear but the effective interaction length will be short.

To increase the interaction length we can use collinear interaction of orthogonally polarized waves in the birefringent nonlinear crystal that is well-known from nonlinear optics of media with quadratic nonlinearity where phase-matched three-wave mixing can be insensitive to the angular mismatch if not only the wave mismatch but also the walk-off effect are compensated using special type of phase matching so-called as tangential phase matching [13–15]. Now we apply this idea in nonlinear optics of media with cubic nonlinearity to increase

FWM anti-Stokes conversion efficiency in the parametric Raman laser.

Let's consider FWM of orthogonally polarized Raman components in the birefringent Raman active crystal. For the first time it was realized in [8] using two input waves called the pump and probe waves with different frequencies, orthogonal polarizations, and separate control of its incidence angle to the crystal. We will simplify this scheme using equal frequencies of the input pump and probe orthogonally polarized waves that requires only one pump laser source. So the pump ordinary wave with the wavelength of λ_L gives us SRS generation of the Stokes ordinary wave with the wavelength of λ_S that is required for coherent stimulation of vibrations of the medium, and the probe extraordinary wave with the wavelength of λ_L will be scattered into the anti-Stokes extraordinary wave with the wavelength of λ_A as a result of interaction with the stimulated vibrations of the medium. As before we can compensate the FWM wave mismatch by control of the pump and Stokes waves propagation directions. Additionally now we can control the propagation direction of the probe and anti-Stokes extraordinary waves to compensate the walk-off of these extraordinary waves beams. Therefore the FWM interaction angular mismatch diagram presented in Fig. 2 shows not only angular mismatch $\Delta\Theta$ between the pump and Stokes ordinary wave vectors $\mathbf{k}_L^o$ and $\mathbf{k}_S^o$, but also angular mismatch $\Delta\beta$ between the pump ordinary wave
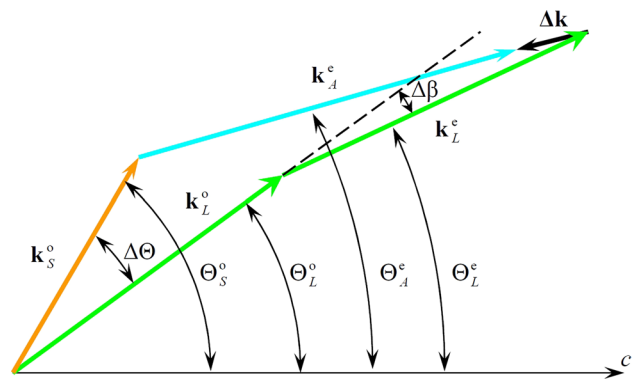

Fig. 2 A FWM interaction angular mismatch diagram of orthogonally polarized Raman components

$$m(\Delta\Theta) = \sqrt{(k_L^o)^2 + (k_S^o)^2 - 2\,k_L^o \cdot k_S^o \cdot \cos\Delta\Theta};$$

$$\delta(\Delta\Theta) = \arccos[(k_L^o - k_S^o \cdot \cos\Delta\Theta)/m(\Delta\Theta)];$$

$$k_{L,S}^o = 2\pi \cdot \lambda_{L,S}^{-1} \cdot n_{L,S}^o;$$

$$k_L^e = 2\pi \cdot \lambda_L^{-1} \cdot n_L^e \cdot n_L^o / \sqrt{(n_L^o)^2 - [(n_L^o)^2 - (n_L^e)^2] \cdot \cos^2\Theta_L^e};$$

$$k_A^e(\Delta\Theta) = 2\pi \cdot \lambda_A^{-1} \cdot n_A^e \cdot n_L^o / \sqrt{(n_A^o)^2 - [(n_A^o)^2 - (n_A^e)^2]\cos^2\Theta_A^e(\Delta\Theta)};$$

$$\Theta_A^e(\Delta\Theta) = \Theta_L^e$$
$$-\arctan \frac{[k_S^o \cdot \sin\Delta\Theta - \sqrt{m(\Delta\Theta)^2 - (k_S^o \cdot \sin\Delta\Theta)^2} \cdot \tan\Delta\beta] \cdot \cos\Delta\beta}{\sqrt{(k_L^e)^2 + m(\Delta\Theta)^2 + 2k_L^e \cdot m(\Delta\Theta) \cdot cos(\delta(\Delta\Theta) \pm \Delta\beta)}};$$

vector $\mathbf{k}_L^o$ and the probe extraordinary wave vector $\mathbf{k}_L^e$. The anti-Stokes (extraordinary) wave ($\mathbf{k}_A^e$) is directed as before to minimize the wave mismatch absolute value Δk. All wave propagation direction angles ($\Theta_{L,S,A}^{o,e}$) in Fig. 2 are given relative to the uniaxial crystal optical axis c, and so $\Delta\Theta = \Theta_S^o - \Theta_L^o$ and $\Delta\beta = \Theta_L^o - \Theta_L^e$.

According to Fig. 2 we find the theoretical expression of the wave mismatch Δk dependence on the angle $\Delta\Theta = \Theta_S^o - \Theta_L^o$ between the Stokes and pump waves:

$$\Delta k(\Delta\Theta) = k_A^e(\Delta\Theta)$$
$$- \sqrt{(k_L^e)^2 + m(\Delta\Theta)^2 + 2\,k_L^e \cdot m(\Delta\Theta) \cdot \cos(\delta(\Delta\Theta) \pm \Delta\beta)}, \tag{10}$$

where

the sign "–" is for $\Delta\Theta > 0$, and the sign "+" is for $\Delta\Theta < 0$.

The angles Θ_L^o and Θ_L^e are the input (controllable) parameters, $n_{L,S,A}^{o,e}$ are the principal values of refractive indices for ordinary (o) and extraordinary (e) waves at the wavelengths of λ_L, λ_S, and λ_A respectively.

We are interested in collinear interaction of the beams which is expected to be insensitive to the angular mismatch, and so we set the pump angle Θ_L^o corresponding to phase matching condition ($\Delta k = 0$) at $\Delta\Theta = 0$. Such phase matching can be conditionally called quasi-collinear because the wave vectors $\mathbf{k}_L^o$ and $\mathbf{k}_S^o$ of biharmonic pumping (the pump and Stokes waves having frequency difference equal to the Raman frequency ν_R) are collinear ($\Delta\Theta = 0$). It is a naturally selected case because the Stokes beam

Fig. 3 Theoretical dependencies of the wave mismatch Δk on the angle $\Delta\Theta$ between the Stokes and pump waves at the pump angle Θ_L^o corresponding to the quasi-collinear phase matching ($\Delta k = 0$ at $\Delta\Theta = 0$) and the angle **a** $\Delta\beta = 0\,^\circ$, **b** 1.7 $^\circ$, **c** 2.3 $^\circ$, **d** 2.6 $^\circ$, **e** 2.9 $^\circ$, and **f** 3.4 $^\circ$ for the CaCO$_3$ crystal under pumping at the wavelength of $\lambda_L = 532$ nm
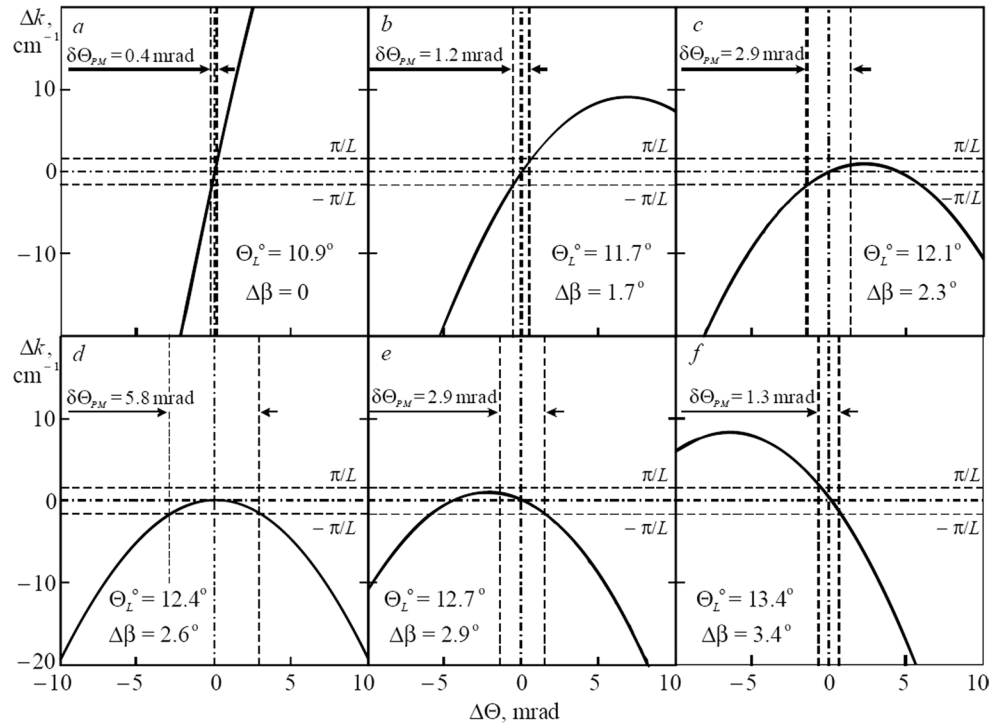
SRS generation is the most efficient at collinear propagation with the pump beam. If the probe wave is collinear too ($\Delta\beta = 0$) this phase matching will be really collinear, but controlling the angle $\Delta\beta$ we are looking for the tangential phase matching insensitive to the angular mismatch at compensation of the walk-off angle of the Poynting vectors of the extraordinary (probe or anti-Stokes) waves [16]

$$\beta_{L,A} = \pm \arctan[(n_{L,A}^o / n_{L,A}^e)^2 \cdot \tan\Theta_{L,A}^e] \mp \Theta_{L,A}^e, \qquad (11)$$

where $\beta_{L,A}$ is the walk-off angle for the probe and anti-Stokes waves respectively, the upper signs refer to a negative crystal and the lower signs to a positive one. Figure 3 presents theoretical dependencies of the wave mismatch Δk on the angle $\Delta\Theta$ between the Stokes and pump waves calculated from the expression (10) at the pump angle Θ_L^o corresponding to the quasi-collinear phase matching ($\Delta k = 0$ at $\Delta\Theta = 0$) and the angle $\Delta\beta = 0°$ (Fig. 3a), 1.7° (Fig. 3b), 2.3° (Fig. 3c), 2.6° (Fig. 3d), 2.9° (Fig. 3e), and 3.4° (Fig. 3f) for the CaCO$_3$ crystal under pumping at the wavelength of $\lambda_L = 532$ nm. Refractive index data for the CaCO$_3$ crystal are taken from [17]. In Fig. 3 there are also shown the values of the angular tolerance of phase matching $\delta\Theta_{PM}$ (vertical dotted lines) taken as doubled value of the least (positive or negative) angular mismatch, i.e. $\delta\Theta_{PM} = 2\delta\Theta_{PM}^{(\pm)}$, where we took sign "+" if $\delta\Theta_{PM}^{(+)} < \delta\Theta_{PM}^{(-)}$, and we took sign "−" if $\delta\Theta_{PM}^{(+)} > \delta\Theta_{PM}^{(-)}$; the angular mismatches $\delta\Theta_{PM}^{(\pm)}$ correspond to $\Delta k = \pm\,\pi/L$ at $L = 2$ cm (horizontal dotted lines).

It can be seen from Fig. 3 that the dependence (10) of Δk on $\Delta\Theta$ for orthogonally polarized waves as for the case of equally polarized waves (the expression (3)) is close to the negative parabola, but position of the parabola peak can be controlled by changing the angles Θ_L^o and $\Delta\beta$.

Changing the angle $\Delta\beta$ gives us the horizontal shift of the parabola $\Delta k(\Delta\Theta)$, and changing the angle Θ_L^o results in its vertical shift, therefore the optimum values of Θ_L^o and $\Delta\beta$ are available corresponding to the quasi-collinear tangential phase matching insensitive to the angular mismatch that is demonstrated by Fig. 3d. So, if the angular tolerance of phase matching is low of about $\delta\Theta_{PM} = 0.4$ mrad at $\Delta\beta = 0$ (Fig. 3a), an increase of the angle $\Delta\beta$ (Fig. 3b–d) with the angle Θ_L^o adjustment to the quasi-collinear phase matching ($\Delta k = 0$ at $\Delta\Theta = 0$) leads to the parabola peak displacement towards the point of origin ($\Delta\Theta = 0$, $\Delta k = 0$) with increasing the angular tolerance of phase matching $\delta\Theta_{PM}$ up to the maximum value of $\delta\Theta_{PM} = 5.8$ mrad (for $L = 2$ cm) at the optimum values $\Theta_L^o = 12.4°$ and $\Delta\beta = 2.6°$ (Fig. 3d) corresponding to placement of the parabola peak at the point of origin. At further increasing the angle $\Delta\beta$ (with adjustment of the angle Θ_L^o to the quasi-collinear phase matching) the parabola movement is mirrored relative to the ordinate axis (Fig. 3, e, f). It is necessary to note that the obtained optimum values ($\Theta_L^o = 12.4\,°$ and $\Delta\beta = 2.6\,°$) correspond to compensation of walk-off of the generated anti-Stokes beam, i.e. $(\Theta_L^o - \Theta_A^e) - \beta_A = 0$, where the anti-Stokes walk-off angle β_A is defined by expression (11). In these
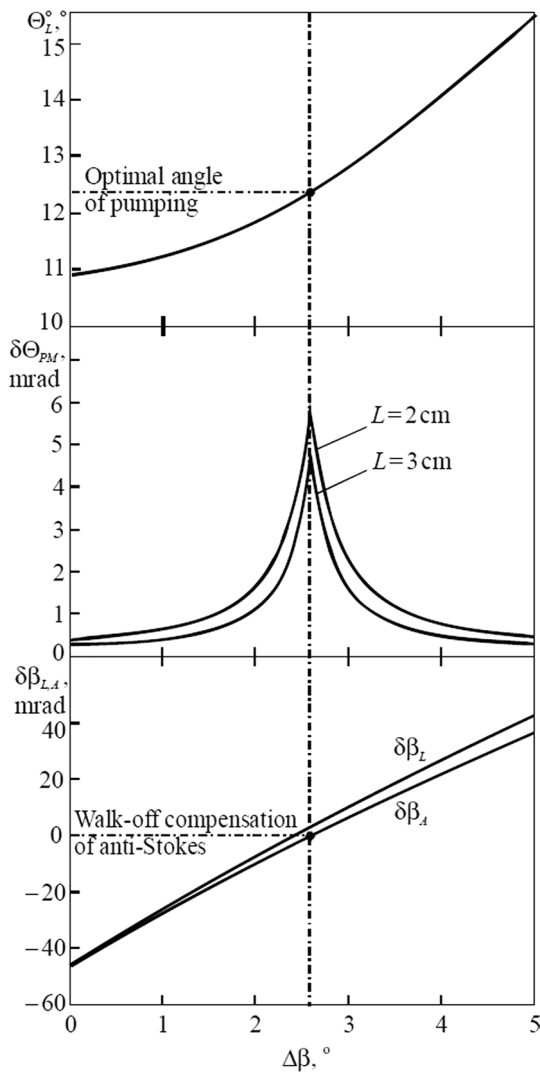
Fig. 4 Theoretical dependencies of the pump angle Θ_L^o corresponding to the quasi-collinear phase matching ($\Delta k = 0$ at $\Delta\Theta = 0$), the angular tolerance of phase matching $\delta\Theta_{PM}$ (for $L = 2$ and 3 cm), and the angle of walk-off compensation $\delta\beta_{L,A} = (\Theta_L^o - \Theta_{L,A}^e) - \beta_{L,A}$ of the probe ($\delta\beta_L$) and anti-Stokes ($\delta\beta_A$) waves on the angle $\Delta\beta$ between the pump and probe waves for the CaCO$_3$ crystal under pumping at the wavelength of $\lambda_L = 532$ nm

conditions the tangential phase matching of four-wave mixing insensitive to the angular mismatch takes place that is similar to the tangential phase matching of three-wave mixing in nonlinear optics of media with quadratic nonlinearity [13–15].

Figure 4 shows the theoretical dependencies of the pump angle Θ_L^o corresponding to the quasi-collinear phase matching ($\Delta k = 0$ at $\Delta\Theta = 0$), the angular tolerance of phase matching $\delta\Theta_{PM}$ (for $L = 2$ and 3 cm), and the walk-off compensation angle $\delta\beta_{L,A} = (\Theta_L^o - \Theta_{L,A}^e) - \beta_{L,A}$ of the probe ($\delta\beta_L$) and anti-Stokes ($\delta\beta_A$) waves on the angle $\Delta\beta$ between the pump and probe waves for the CaCO$_3$ crystal under pumping at the wavelength of $\lambda_L = 532$ nm.

As one can see the sharp growth of the angular tolerance of phase matching up to the maximum of $\delta\Theta_{PM} = 5.8$ mrad at $L = 2$ cm and $\delta\Theta_{PM} = 4.7$ mrad at $L = 3$ cm takes place at the optimal values of $\Theta_L^o = 12.4°$ and $\Delta\beta = 2.6°$ corresponding to the exact anti-Stokes wave ($\delta\beta_A = 0$) walk-off compensation. However walk-off for the probe wave at the optimum is not completely compensated and the compensation angle amounts $\delta\beta_L = 3.4$ mrad. It slightly limits the effective interaction length by the value of $L_{\delta\beta} \approx d_0/\delta\beta_L$, where d_0 is the beam diameter, that is similar to the effective length $L_\beta \approx d_0/\beta_L$ limited by walk-off, but $L_{\delta\beta}$ is approximately 10 times higher than L_β. For example, at $d_0 = 140$ μm we get $L_{\delta\beta} = 4$ cm against $L_\beta = 0.33$ cm, i.e. we can use here a long CaCO$_3$ crystal even for the strongly focused beam.

Thus, from the theoretical study we can formulate the conclusion that phase matching of parametric Raman interaction is insensitive to the angular mismatch if the Poynting vectors for the biharmonic pump waves and for the parametrically generated (anti-Stokes) component are collinear.

3 Mathematical modeling of the phase-matched anti-Stokes generation in the parametric Raman laser at collinear interaction of orthogonally polarized Raman components

In contrast to the simple case of the Stokes-anti-Stokes parametric Raman interaction of equally polarized waves [1–7] we have here two orthogonally polarized optical channels (pump and probe channels) for the Stokes (ordinary wave) and anti-Stokes (extraordinary wave) generation separately from the pump and probe beams described by the coupled wave equations

$$\frac{\partial E_L^o}{\partial z} + \frac{1}{u_L^o}\frac{\partial E_L^o}{\partial t} = -i\,\frac{\pi\,\omega_L^2}{k_L^o\,c^2}\,N\,\frac{\partial\alpha}{\partial Q}\left(E_S^o\,q_{LS} + E_S^o\,q_{AL}\,e^{-i\,\Delta k\,z}\right),$$
$$\frac{\partial E_L^e}{\partial z} + \frac{1}{u_L^e}\frac{\partial E_L^e}{\partial t} = -i\,\frac{\pi\,\omega_L^2}{k_L^e\,c^2}\,N\,\frac{\partial\alpha}{\partial Q}\left(E_A^e\,q_{AL}^* + E_A^e\,q_{LS}^*\,e^{-i\,\Delta k\,z}\right),$$
$$\frac{\partial E_S^o}{\partial z} + \frac{1}{u_S^o}\frac{\partial E_S^o}{\partial t} = -i\,\frac{\pi\,\omega_S^2}{k_S^o\,c^2}\,N\,\frac{\partial\alpha}{\partial Q}\left(E_L^o\,q_{LS}^* + E_L^o\,q_{AL}^*\,e^{i\,\Delta k\,z}\right),$$
$$\frac{\partial E_A^e}{\partial z} + \frac{1}{u_A^e}\frac{\partial E_A^e}{\partial t} = -i\,\frac{\pi\,\omega_A^2}{k_A^e\,c^2}\,N\,\frac{\partial\alpha}{\partial Q}\left(E_L^e\,q_{AL} + E_L^e\,q_{LS}\,e^{i\,\Delta k\,z}\right),$$

$$(12)$$

and material equations

$$\frac{\partial q_{LS}}{\partial t} + \frac{1}{\tau}\cdot q_{LS} = -\frac{i}{4\cdot m\cdot\Omega}\cdot\frac{\partial\alpha}{\partial Q}\cdot E_L\cdot E_S^*,$$
$$\frac{\partial q_{AL}}{\partial t} + \frac{1}{\tau}\cdot q_{AL} = -\frac{i}{4\cdot m\cdot\Omega}\cdot\frac{\partial\alpha}{\partial Q}\cdot E_A\cdot E_L^*,$$

$$(13)$$

where $E_{L,S,A}^{o,e}$ are the slowly varying amplitudes of the respective radiation components, $\omega_{L,S,A}$ and $u_{L,S,A}^{o,e}$ are the optical frequency and the group velocity of the respective radiation components, q_{LS} is the slowly varying amplitude of the medium vibrations forced by the E_L^o and E_S^o wave

interference, q_{AL} is the slowly varying amplitude of the medium vibrations forced by the E_L^e and E_A^e wave interference, m and N are the effective mass and concentration of vibrating particles, $\partial \alpha / \partial Q$ is the coefficient of change of the polarizability of the medium, τ is the vibrational dephasing time. The derivation of Eqs. (12)–(13) is the same as in [18].

In Eqs. (12)–(13) we took into account equal values of nonlinear coefficients for Raman and parametric interactions. We need to make this approximation because the $\partial \alpha / \partial Q$ coefficient is a tensor describing the coupling between orthogonally polarized waves. For calcite crystal having symmetry group of $\bar{3}m$, the $\partial \alpha / \partial Q$ tensor of the totally symmetric Raman active vibration ($A_{1\,g}$) is [19]

$$\left(\frac{\partial \alpha}{\partial Q} \right)_{A_{1g}} = \begin{pmatrix} a & 0 & 0 \\ 0 & a & 0 \\ 0 & 0 & b \end{pmatrix}, \qquad (14)$$

and the nonlinear coupling coefficient is proportional to a^2 if the coupled waves are all ordinary waves (Raman interaction in the pump channel), however the nonlinear coupling coefficient is proportional to $a^2 \cos^2 \Theta + ab \sin^2 \Theta$ if the pump and Stokes waves are ordinary waves, but the probe and anti-Stokes waves are extraordinary waves (parametric interaction between the pump and probe channels) where Θ is the angle of light propagation relative to the crystal optical axis. Having the pump angle of $\Theta_L^o = 12.4°$ (see Fig. 4a) and $b << a$ [20] for the CaCO$_3$ crystal, we obtain $a^2 \cos^2 \Theta + ab \sin^2 \Theta \approx 0.95\,a^2$ which is close to the value (a^2) for the ordinary wave Raman interaction in the pump channel, and so we can use equal coefficients for Raman and parametric coupling in the model (12)–(13).

In the model we didn't taken into account Raman generation of the first Stokes component in the probe channel and the second Stokes component in the pump channel, and so the model can be used at the probe pulse intensity I_{probe} lower than the Raman threshold value I_{th} [11] in the probe channel and at the pump pulse energy I_{pump} lower than the doubled Raman threshold value $2I_{th}$ in the pump channel.

Figure 5 demonstrates the numerical simulation results of the Eqs. (12)–(13) describing the parametric Raman generation in the 2-cm long CaCO$_3$ crystal (Raman gain of 13 cm/GW, Raman frequency of 1086 cm^{-1}, vibrational dephasing time of 8.8 ps) at phase matching ($\Delta k = 0$) under pumping and probing at the wavelength $\lambda_L = 532$ nm, the pulse duration $t_L = 20$ ps, the pump pulse intensity I_{pump} by 2 times higher than the Raman threshold, and the probe pulse intensity $I_{probe} = 0.05I_{pump}$ (Fig. 5a), $I_{probe} = 0.26I_{pump}$ (Fig. 5b), and $I_{probe} = 0.35I_{pump}$ (Fig. 5c).

It can be seen from Fig. 5, increasing the probe pulse intensity from $I_{probe} = 0.05I_{pump}$ (Fig. 5a) up to $I_{probe} = 0.35I_{pump}$ (Fig. 5c) results in decreasing the
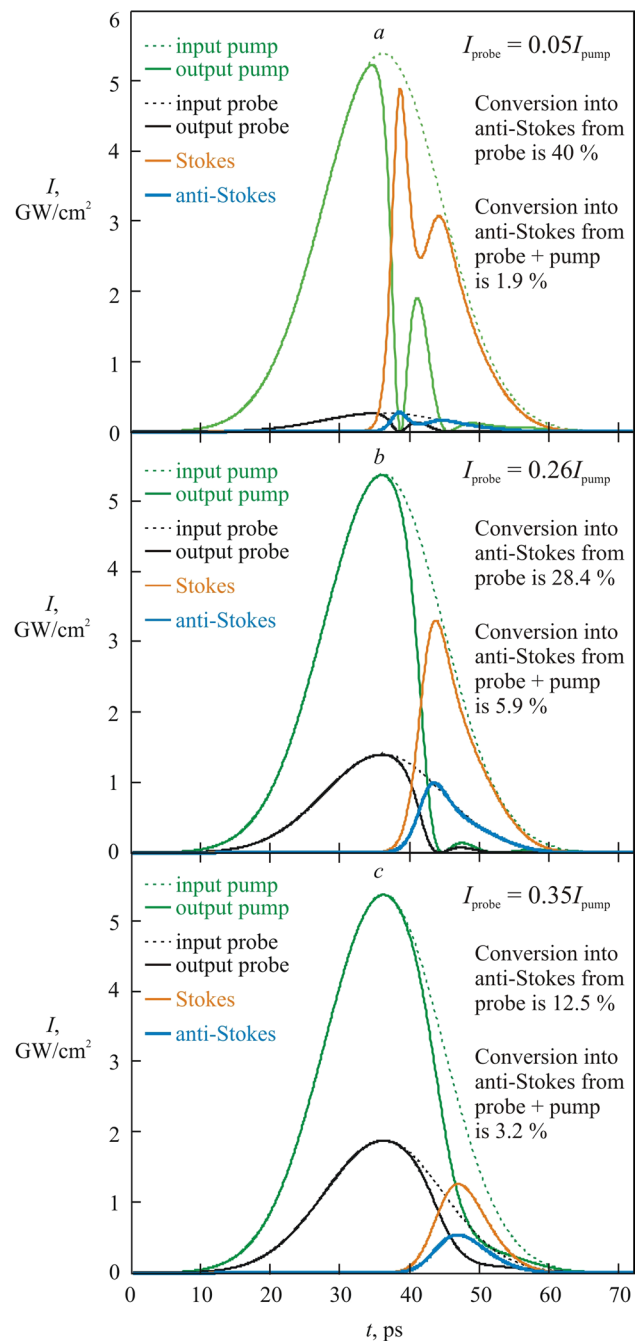

Fig. 5 The numerical simulation results of the parametric Raman generation in the 2-cm long CaCO$_3$ crystal under pumping and probing at the wavelength $\lambda_L = 532$ nm, the pulse duration $t_L = 20$ ps, the pump pulse intensity I_{pump} 2 times higher than the Raman threshold, and the probe pulse intensity $I_{probe} = 0.05I_{pump}$ (a), $I_{probe} = 0.26 I_{pump}$ (b), and $I_{probe} = 0.35I_{pump}$ (c)

conversion into the anti-Stokes wave from the probe wave from 40 to 12.5%. It can be explained in the following way. Analysis of the system (12) shows that parametric generation of the anti-Stokes wave (E_A^e) from the probe wave (E_L^e) takes place on the medium vibrations

(q_{LS}) forced by another pair of waves (E_L^o and E_S^o) (see last terms of second and fourth equations). On the contrary parametric coupling of the pump (E_L^o) and Stokes (E_S^o) waves occurs by means of the medium vibrations forced by the anti-Stokes (E_A^e) and probe (E_L^e) waves (see last terms of first and third equations). Increasing the probe wave intensity at phase matching ($\Delta k = 0$) leads to increasing the vibration amplitude q_{AL} up to the vibration amplitude q_{LS}, but these vibrations have a phase shift of π, and so they coherently subtract each other that results in suppression of forced vibrations of the medium and then suppression of both the Stokes and anti-Stokes parametric Raman generation.

It can also be seen that overall optical efficiency of the anti-Stokes generation from both the probe and pump waves has the maximum value of 5.9% at the optimal probe pulse energy of $I_{probe} = 0.26 I_{pump}$ (Fig. 5b).

The modeling also shows that increasing the pump pulse intensity I_{pump} leads to increasing the highest conversion efficiency into the anti-Stokes wave from the probe wave (at $I_{probe} << I_{pump}$) and also increasing the optimal probe pulse energy for the maximal overall generation efficiency of the anti-Stokes wave from both the probe and pump waves. However at the pump pulse intensity $I_{pump} > 2I_{th}$ the second Stokes Raman conversion should be generated decreasing the generation efficiency of the anti-Stokes wave. So, the pump pulse intensity should be $I_{pump} < 2I_{th}$ for efficient anti-Stokes generation.

4 Experimental study of the anti-Stokes generation of the parametric Raman laser at collinear interaction of orthogonally polarized Raman components in CaCO$_3$ crystals under excitation by the 532-nm frequency-doubled picosecond Nd:YAG laser

As a laser pump source, a laboratory-designed oscillator-amplifier 532-nm frequency-doubled picosecond Nd:YAG laser system was used. The quasi-continuous laser-diode pumped laser oscillator was based on a 2.4 at.%-doped Nd:YAG active crystal and passively mode-locked by a semiconductor saturable absorber. Linearly polarized 20 ps single pulses extracted from the oscillator were further amplified using two flashlamp-pumped Nd:YAG amplifiers to the energy level of ~10 mJ. The repetition rate was limited by the power supply to 10 Hz. The second harmonic generator (a 30-mm KDP crystal) was used and the radiation polarization was adjusted in order to generate the 532-nm laser radiation linearly polarized at 45° from the horizontal plane. The oscillator details are described in [11].

We propose a new scheme of the crystalline parametric Raman anti-Stokes laser presented in Fig. 6. The parametric Raman laser consists of the laser pump source (1); the birefringent prism (2) splitting the laser pump source radiation into two orthogonally polarized beams—one represents the pump beam and the second the probe beam; the

Fig. 6 Crystalline parametric Raman anti-Stokes laser schematic: (1) laser pump source, (2) birefringent prism, (3–6) total reflection prisms, (7) wide-aperture objective, (8) parametric Raman laser active crystal. Inset left: measured pump (532 nm) and Stokes (565 nm) beam spatial profiles. Inset right: measured pump (532 nm) and anti-Stokes (503 nm) beam spatial profiles
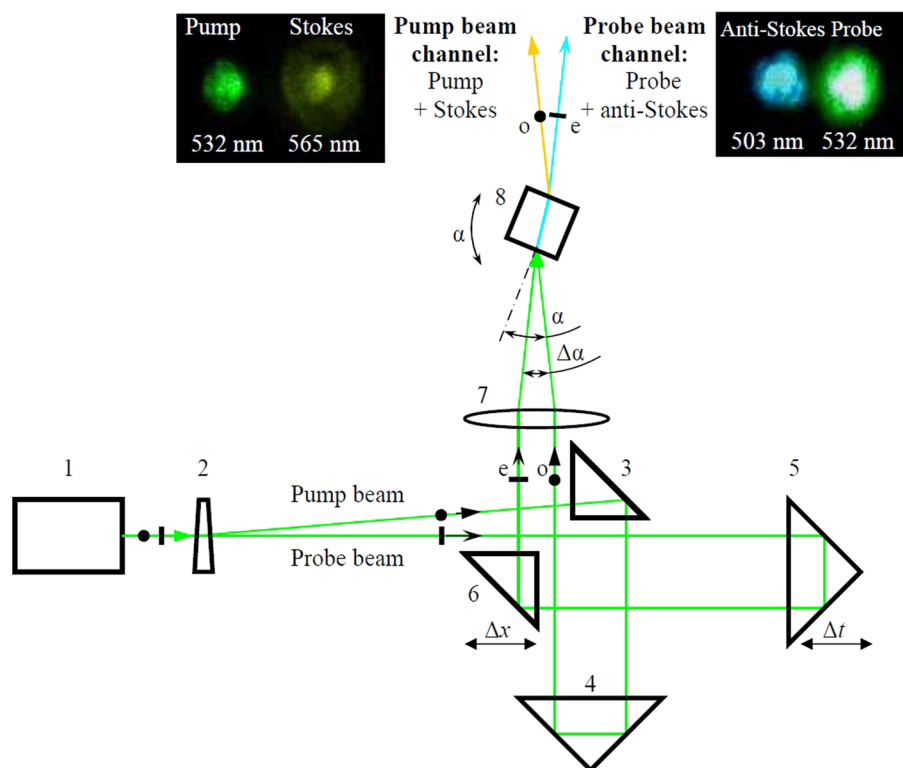
total reflection prisms (3–6) directing the pump and probe beams into the parametric Raman laser active crystal; the wide-aperture objective (7) focusing the parallel pump and probe beams into the active crystal of the parametric Raman laser; the parametric Raman laser active crystal (8) being the birefringent Raman-active crystal. The prisms (5) and (6) are also used to control the temporal (linear translation of the prism (5) to control the probe pulse delay Δt) and spatial (linear translation Δx of the prism (6) to control the angle $\Delta \alpha$ between the pump and probe beams) overlaps of the pump and probe beams in the active crystal (8), and therefore these prisms are placed on the precise translation stages. To control the incidence angle α of the pump beam, the active crystal (8) is placed on the precise rotation stage with the rotation axis lying in a plane of the input face of the active crystal (8). The input face of the active crystal (8) is also placed in the objective focus (7). The pump and probe beams should be precisely parallel before incidence on the objective (7) to get its intersection after focusing at the active crystal (8) input face, and therefore the prism (6) is also placed on a precise translation and rotation stage. To vary the pump and probe pulse energies, variable transmittance filters were employed.

As the active crystal (8) of the parametric Raman laser, a c-cut $CaCO_3$ crystal was used. We examined two $CaCO_3$ crystal samples with the lengths of 2.1 and 3.2 cm. In the optical scheme in Fig. 6 the optical axis of the active $CaCO_3$ crystal is perpendicular to its rotation axis, and the incident pump wave polarization is oriented perpendicular to the optical axis of the active $CaCO_3$ crystal for ordinary wave pumping. The external angles α and $\Delta \alpha$ controlled in the experiment are coupled by the law of refraction with the relative internal angles Θ_L^o and $\Delta \beta$ considered in the theoretical study.

As the focusing objective (7) we used one or two closely spaced wide-aperture (> 5 cm) positive lenses with the focal lengths of $f_1 = 365$ mm and $f_2 = 500$ mm, that allows to change the focal length f of the objective (7): $f = 1/(1/f_1 + 1/f_2) = 211$ mm using both lenses, $f = f_1 = 365$ mm using the first lens only, and $f = f_2 = 500$ mm using the second lens only.

At the pump wavelength of $\lambda_L = 532$ nm (green radiation) the Stokes and anti-Stokes components generating in the $CaCO_3$ crystal ($\nu_R = 1086$ cm^{-1}) have wavelengths of $\lambda_S = 565$ nm (yellow radiation) and $\lambda_A = 503$ nm (cyan radiation).

In order to measure the yellow Stokes radiation, a long-pass filter (Thorlabs FEL550) was used to block the pumping radiation at $\lambda_L = 532$ nm and transmit the Stokes radiation ($T = 88\%$ @ $\lambda_S = 565$ nm).

For separate cyan (503 nm) anti-Stokes radiation measurement two dispersion SF6 glass prisms were used. The pulse energy was precisely measured by the energy probe

Coherent J-10MB-LE (0.2–600 µJ) connected to the energy meter Coherent FieldMax II. Lower energies (< 0.2 µJ) were measured using the calibrated large-aperture photodiode Thorlabs FDS1010. To achieve synchronization of the pump and probe pulses in the active crystal, the temporal measurement was carried out using the photodiode EOT ET-3500 (analog bandwidth > 12.5 GHz) connected to the oscilloscope LeCroy SDA 9000 (analog bandwidth 9 GHz). Spectral parameters were measured by the spectrometer OceanOptics HR2000 (wavelength range 200–1100 nm, resolution < 2 nm). The beam spatial profiles were measured using the CCD camera WinCamD.

At first we used the focusing objective with the focal length of $f = 211$ mm (the two-lens objective) and the 2.1 cm long active $CaCO_3$ crystal. The pump and probe beams focused by the objective had similar angular divergence of 8.6 mrad outside the active crystal (5.2 mrad inside the active crystal) with the beam quality of $M^2 = 1.4$. A minimal diameter of the focused pump and probe beams was as low as $d_0 = 0.11$ mm (at 13.5%), and the beam waist Rayleigh length was as long as $L_R = \pi d_0^2 n_0 / 4 \lambda_L M^2 \approx 2.1$ cm in the crystal medium that is close to the crystal length. At the pump pulse energy higher than 12 µJ (independent on the probe pulse energy) in the pump beam channel (see Fig. 6) the Stokes SRS generation threshold at the wavelength of $\lambda_S = 565$ nm was achieved.

Using the rotation stage the active $CaCO_3$ crystal was rotated relative to normal incidence to the angle close to the theoretical optimum angle of incidence $\alpha = \arcsin(n_L^o \cdot \sin \Theta_L^o) \approx 20.9$ ° at $n_L^o = 1.663$ and $\Theta_L^o = 12.4$° (see the theoretical study). Using the prism (6) (Fig. 6) linear translation the distance between the parallel pump and probe beams (incident to the focusing objective (7)) was adjusted close to the theoretical optimum value corresponding to the walk-off compensation: $\Delta x = \Delta \alpha \cdot f \approx 17$ mm, where $f = 211$ mm, $\Delta \alpha = \alpha - \arcsin[n_L^e(\Theta_L^o - \Delta \beta) \cdot \sin(\Theta_L^o - \Delta \beta)] \approx 4.5°$ at $n_L^e(\Theta_L^o - \Delta \beta) = 1.657$, $\Theta_L^o = 12.4$° and $\Delta \beta = 2.6$° (see the theoretical study). It allowed to register axial generation of the cyan anti-Stokes radiation with the wavelength of $\lambda_A = 503$ nm in the probe beam channel that was achieved by decomposing the light into a spectrum by the dispersion prisms. Fine adjustment of the temporal and spatial overlaps using linear translation of prisms (5) and (6) (Fig. 6) allowed to maximize the anti-Stokes radiation intensity. Thereby the spatial overlap (walk-off compensation) was visually controlled by overlap of spots of the pump and probe beams at the output face of the active crystal.

Figure 7 demonstrates spectral and spatial parameters of radiation in the probe beam channel at the optimal conditions of adjustment of phase matching ($\alpha_0 = 20.9$°), spatial ($\Delta \alpha_0 = 4.5$°), and temporal ($\Delta t = 0$) overlaps of the pump

Fig. 7 Radiation spectrum and spatial beam profiles of optical components decomposed by the dispersion prisms in the probe beam channel at the optimal conditions of phase matching adjustment ($\alpha_0 = 20.9°$), spatial ($\Delta\alpha_0 = 4.5°$), and temporal ($\Delta t = 0$) overlaps of the pump and probe beams at the pump and probe pulse energy of 23 and 2 μJ, respectively
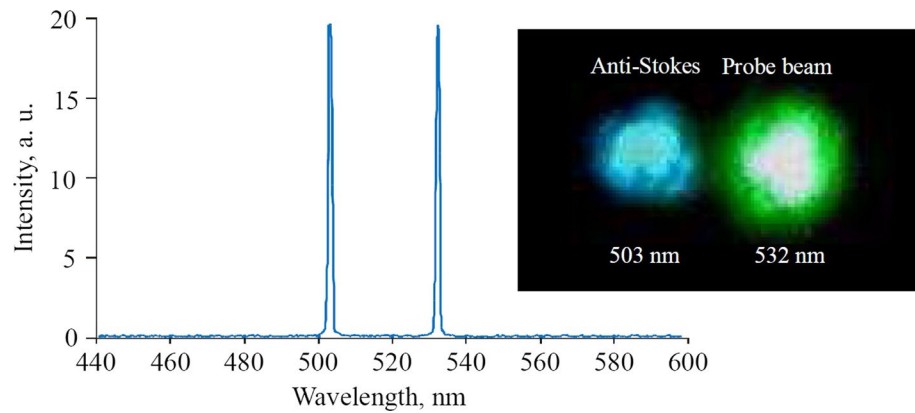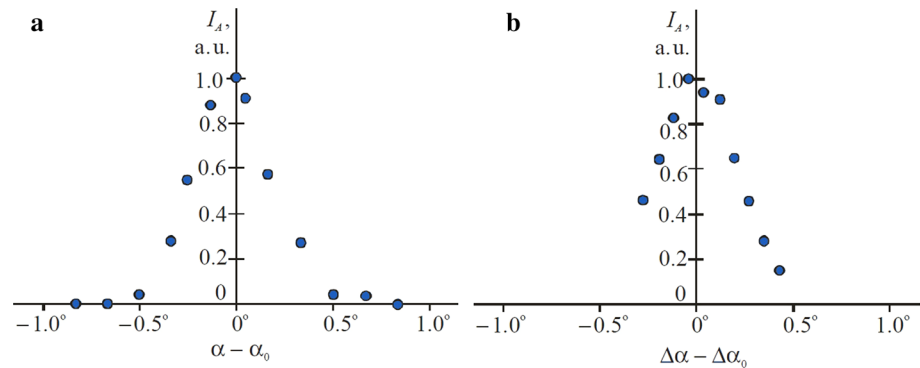

Fig. 8 The angular mismatch characteristics for the anti-Stokes generation intensity in dependence on the angles α (a) and $\Delta\alpha$ (b) (initial values $\alpha_0 = 20.9°$, $\Delta\alpha_0 = 4.5°$) at the pump and probe pulse energy of 27 and 7 μJ respectively

and probe beams at the pump and probe pulse energy of 23 and 2 μJ, respectively.

It can be seen that in the probe beam channel there is only the anti-Stokes component generation at the wavelength of 503 nm and conversion efficiency from the probe wave (532 nm) of about 10 %. The relatively small spot of the anti-Stokes radiation and the beam profile close to Gaussian indicate high diffraction-limited quality of the generated anti-Stokes radiation. Note that at the same time in the pump beam channel there was generated only the Stokes component with the wavelength of 565 nm and conversion efficiency from the pump wave of about 26 %, but the spot size of the Stokes beam was essentially (approximately by 1.5 times) higher than the pump beam spot (see the inset in Fig. 6).

Figure 8 shows the angular mismatch characteristics for the anti-Stokes generation intensity in dependence on the angles α and $\Delta\alpha$ ($\alpha_0 = 20.9°$, $\Delta\alpha_0 = 4.5°$) at the pump and probe pulse energy of 27 and 7 μJ respectively. As one can see the tolerable mismatch for both angles α and $\Delta\alpha$ amounts about $\pm0.3°$ being in the agreement with the theoretical tolerable mismatches of corresponding internal angles Θ_L^o and $\Delta\beta$ shown in Fig. 4.

Figure 9 presents the experimental dependencies of the anti-Stokes pulse energy (Fig. 9a), the anti-Stokes conversion efficiency from the probe beam (Fig. 9b), and the

overall optical efficiency of the anti-Stokes generation (Fig. 9c) from both the pump and probe input beams on the probe pulse energy at various values of the pump pulse energy for the 2.1-cm active $CaCO_3$ crystal and the objective focal length of 211 mm.

It can be seen from Fig. 9a that the anti-Stokes energy growth was saturated when the probe pulse energy increased relatively to the pump pulse energy for the pump energies up to 23 μJ and the tendency seems to be similar for the investigated pump energy of 30 μJ. The anti-Stokes conversion efficiency from the probe beam (Fig. 9b) had maximum of 6–12% at low values of the probe pulse energy (< 5 μJ), and increasing the probe pulse energy resulted in decreasing the probe-to-anti-Stokes conversion efficiency down to ~4%. This decrease wasn't connected with the energy losses at the competing process of the Stokes component SRS generation from the probe beam because its generation threshold was higher at the level of about 13 μJ of the probe pulse energy. The energy growth saturation is also demonstrated in the fast saturation of the overall optical efficiency of the anti-Stokes generation (Fig. 9c).

Note that efficient anti-Stokes generation took place in a range of the pump pulse energy from the lowest value of 15 μJ corresponding to a near-threshold SRS regime of the 565-nm (yellow) Stokes SRS generation from the

Fig. 9 The experimental dependencies of **a** the anti-Stokes pulse energy, **b** the anti-Stokes conversion efficiency from the probe beam, and **c** the overall optical efficiency of the anti-Stokes generation from both the pump and probe beams on the probe pulse energy at the various pump pulse energies for the 2.1-cm active $CaCO_3$ crystal and the objective focal length of 211 mm
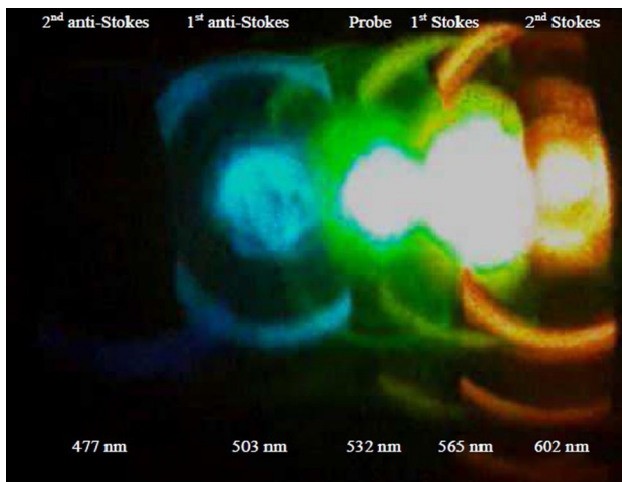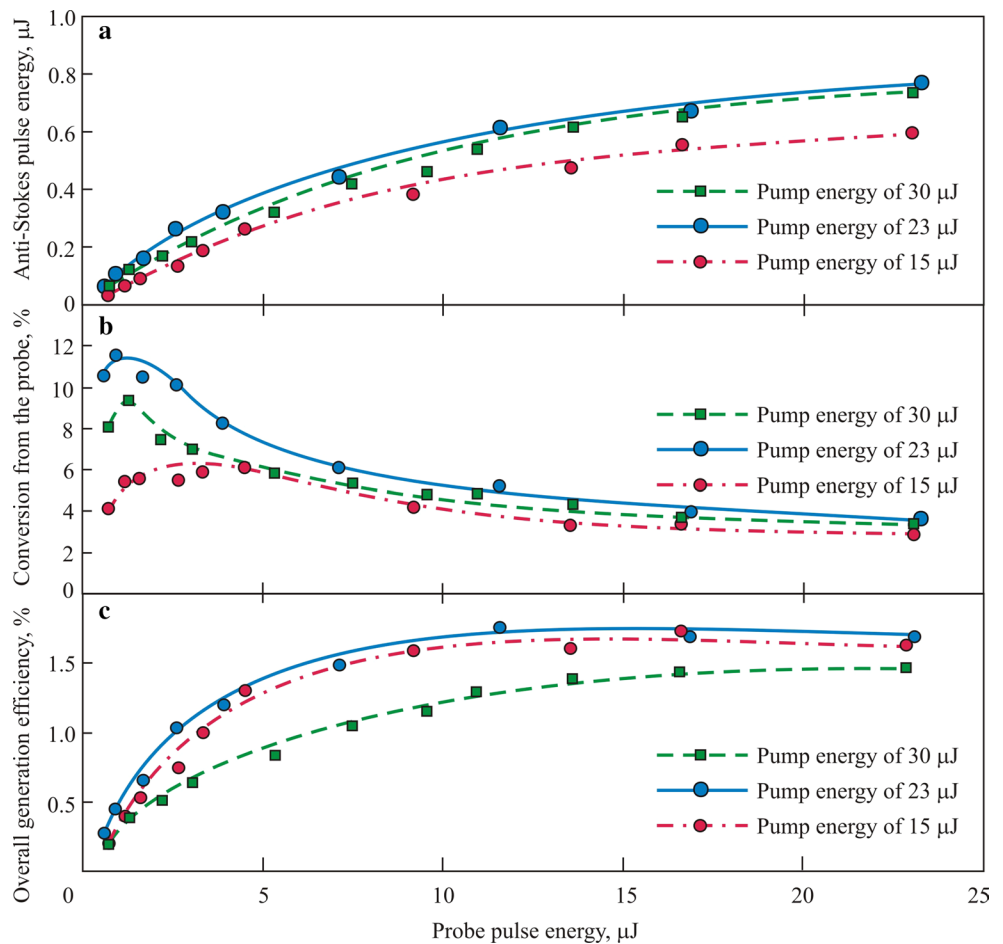

Fig. 10 Photo of optical components decomposed by the dispersion prisms in the probe beam channel at very high and equal pump and probe energies of 45 μJ

pump and probe pulse energies led to decreasing the anti-Stokes generation efficiency because of the energy losses to the competing process of the cascade-like SRS generation. One more problem to increase the axial anti-Stokes energy is phase self-matching for conical generation of Raman components taking place at very high pump and probe pulse energies (45 μJ) that is demonstrated by a photo in Fig. 10.

Saturation of the anti-Stokes energy growth observed even at the probe pulse energies lower than the threshold value of 15 μJ for the Stokes Raman generation from the probe wave can be explained by parametric suppression of both the Stokes and anti-Stokes waves at increasing the probe pulse energy up to the pump pulse energy as it follows from the above mentioned mathematical modeling results (Fig. 5). In our experiment this suppression was not full because the generated Stokes radiation had high beam divergence, and so only its central (paraxial) part took part in the phase-matched parametric Raman interaction.

We measured the beam divergence of the generated components using the iris diaphragm placed at different distances from the laser and measuring the beam diameters containing 86.5% of the radiation energy. The anti-Stokes

pump beam up to the highest value of 30 μJ corresponding to the second Stokes SRS threshold at the wavelength of 602 nm (orange radiation). Further increasing the

beam divergence was as high as 5.9 mrad outside the active crystal (3.6 mrad inside the active crystal)corresponding to the diffraction limit at the minimum diameter equal to the pump beam diameter (0.11 mm). The anti-Stokes beam divergence was constant in the range of the pump and probe pulse energy of 13–20 μJ. At the probe pulse energy higher than 20 μJ in addition to the axial anti-Stokes generation the conical anti-Stokes component (a ring around the central spot) was generated. The anti-Stokes beam divergence is the measure of the angular tolerance of phase matching, therefore it is comparable with its theoretical estimation ($\delta\Theta_{PM} = 5.8$ mrad). Angular divergence of the Stokes SRS radiation in the pump beam channel amounts 13 mrad outside the active crystal (7.8 mrad inside the active crystal) and was constant in the range of the pump pulse energy of 13–20 μJ at the Gaussian beam profile.
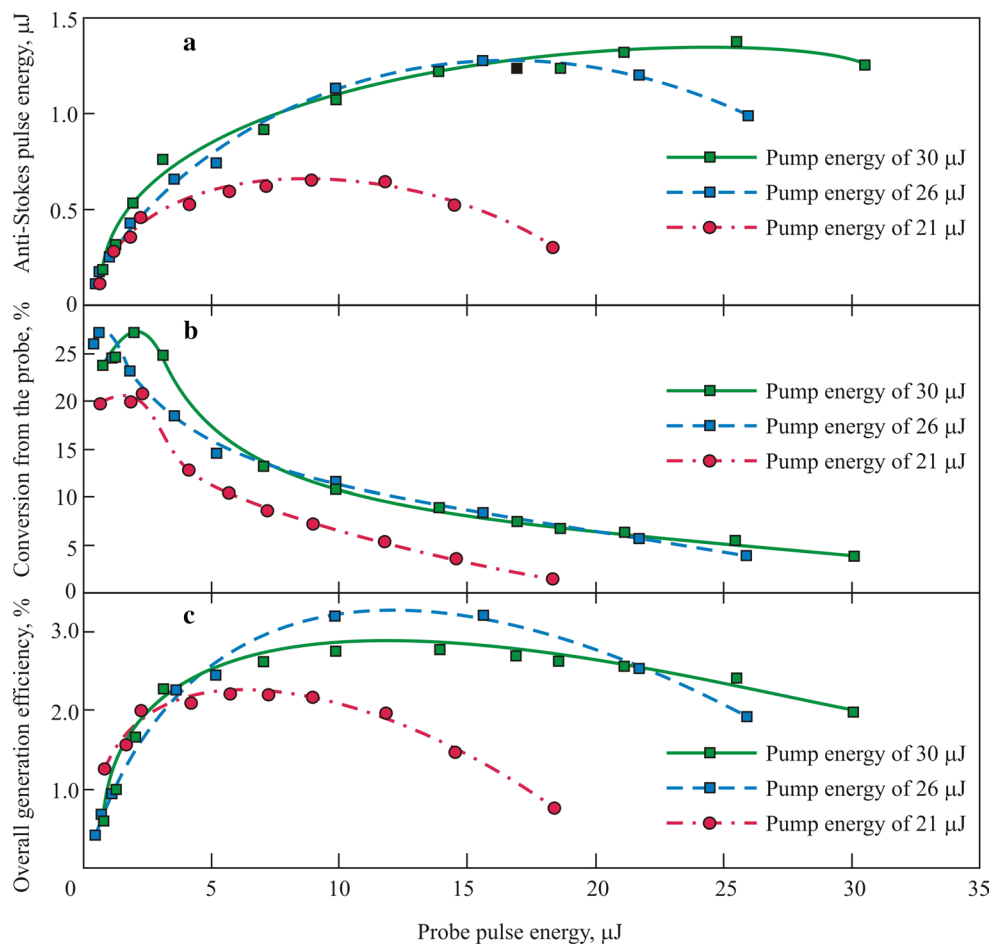
In order to decrease the excitation beam divergence to the value lower than the phase matching angular tolerance we increased the objective focal length from $f = 211$ mm ($f = 1/(1/f_1+1/f_2)$) up to $f = 365$ mm ($f = f_1$). It resulted in decreasing the pump and probe beam divergence from 8.6 mrad outside the active crystal (5.2 mrad inside the active crystal) down to 5.0 mrad outside the active

crystal (3.0 mrad inside the active crystal). The pump and probe beam minimal diameter in the focus was increased to $d_0 = 0.19$ mm at conservation of the beam quality ($M^2 = 1.4$).

However at such pumping of the active $CaCO_3$ crystal with a length of 2.1 cm the generated Stokes beam divergence increased up to 16 mrad outside the active crystal (9.6 mrad inside the active crystal). The Stokes beam divergence inside the active crystal (9.6 mrad) was in the agreement with the geometrical estimation of the acceptance angle of the interaction channel $d_0/L \approx 9$ mrad ($d_0 = 0.19$ mm and $L = 21$ mm). Thus, we had the case of wide beam pumping with the pump beam Rayleigh length of ($L_R = \pi d_0^2 n_0/4\lambda_L M^2 \approx 63$ mm) 3 times higher than the active crystal length ($L = 21$ mm), and so the generated Stokes beam divergence wasn't caused by diffraction, but determined by the acceptance angle of the interaction channel d_0/L.

Under these conditions the anti-Stokes energy and efficiency didn't increase in comparison with the previous case. It can be explained by very high beam divergence of the Stokes SRS radiation (9.6 mrad inside the crystal) exceeding the angular tolerance of phase matching ($\delta\Theta_{PM} = 5.8$ mrad).

Fig. 11 The experimental dependencies of (*a*) the anti-Stokes pulse energy, (*b*) the anti-Stokes conversion efficiency from the probe beam, and (*c*) the overall optical efficiency of the anti-Stokes generation from both the pump and probe beams on the probe pulse energy at the various pump pulse energies for the 3.2-cm active $CaCO_3$ crystal and the objective with focal length of 365 mm

In order to decrease the generated Stokes beam divergence and to increase the anti-Stokes energy we used the second longer $CaCO_3$ crystal with the length of $L = 3.2$ cm. It led to the acceptance angle (d_0/L) decrease down to 6 mrad at the same pumping conditions ($f = 365$ mm). So, the measured divergence of the Stokes beam decreased from 16 mrad (at $L = 2.1$ cm) to 10 mrad (at $L = 3.2$ cm) outside the active crystal that corresponded to decreased beam divergence of 6.0 mrad inside the active crystal (close to d_0/L).

Under given conditions we obtained the best energy characteristics of the anti-Stokes generation presented in Fig. 11. It can be seen that the dependencies character is analogous to one presented in Fig. 9, but all the maximal energy characteristics increased approximately by 2 times: the maximal energy of the anti-Stokes pulse was 1.4 μJ at the pump and probe pulse energy of 30 and 25 μJ, the maximal efficiency of the anti-Stokes conversion from the probe beam was 27% at the pump and probe pulse energy of 30 and 2 μJ, the maximal optical efficiency of the anti-Stokes generation (from both the pump and probe beams) was 3.1% at the pump and probe pulse energy of 26 and 12 μJ. We can also see that the anti-Stokes pulse energy (Fig. 11a) and its generation efficiency (Fig. 11c) had not only saturated growth, but also reached its maximum and then decreased at the probe pulse energy increase in an agreement with the above mentioned mathematical modeling results (Fig. 5). The experimental optimum ratio for pump-probe energy at the pump energy of 21 μJ (that is approximately 2 times higher than Raman threshold in the pump channel) is in a good agreement with the modeling result ($I_{probe}/I_{pump} = 0.26$). The decrease can be explained by stronger suppression of the Stokes-anti-Stokes parametric Raman interaction when the probe energy reached the pump energy in comparison with the previous case due to lower divergence of the generated Stokes beam considering the phase matching angular tolerance. It resulted in faster reduction of the anti-Stokes conversion from the probe beam right down to zero at the pump pulse energy of 21 μJ and the probe pulse energy higher than 18 μJ (Figure 11b).

Note that the investigated $CaCO_3$ crystals had no antireflection coatings, and so we had Fresnel losses (∼5 %) on reflection of the pump and probe beams from the input face of the active crystal, and also on reflection of the anti-Stokes beam from the crystal output face. Taking into account the Fresnel losses the anti-Stokes conversion and generation efficiencies can be increased by a factor of $0.95^{-2} \approx 1.11$, i.e. from 27 to 30% and from 3.1 to 3.5%, then we get the experimental efficiency of the anti-Stokes conversion from the probe wave of 30% being close to the highest modeling result of 40% (Figure 5,a).

Finally, using the objective with the longest focal length of $f = f_2 = 500$ mm didn't allow to increase the energy characteristics of the anti-Stokes generation in spite of decreasing the pump and probe beam divergence because of a significant increase of the generated Stokes beam divergence even using the long 3.2-cm active crystal.

5 Conclusions

In conclusion, the possibilities of increasing the efficiency of parametric Raman generation of the anti-Stokes component at orthogonally polarized FWM using not only phase matching fulfillment, but also the extraordinary waves walk-off compensation in the birefringent Raman-active crystal were theoretically and experimentally studied. It was shown that the phase matching of parametric Raman interaction is tangential and insensitive to the angular mismatch if the Poynting vectors of the biharmonic pump and parametrically generated (anti-Stokes) waves are collinear. For the first time it allows to achieve experimentally the highest conversion efficiency into the anti-Stokes wave (503 nm) up to 30% from the probe wave and up to 3.5% from both pump and probe waves in the single-pass picosecond parametric Raman laser based on the Raman-active calcite crystal under excitation by the single 532 nm laser source.

References

1. C. Reiser, T.D. Raymond, R.B. Michie, A.P. Hickman, Efficient anti-Stokes Raman conversion in collimated beams. J. Opt. Soc. Am. B **6**, 1859–1869 (1989)
2. A.Z. Grasiuk, L.L. Losev, A.P. Lutsenko, S.N. Sazonov, Raman parametric generation of anti-Stokes radiation under conditions of amplification of an external Stokes signal. Sov. J. Quantum Electron. **20**(5), 529–532 (1990)
3. A.Z. Grasiuk, S.V. Kubasov, L.L. Losev, Picosecond parametric Raman laser based on $KGd(WO_4)_2$ crystal. Opt. Comm. **240**, 239–244 (2004)
4. R. Chiao, B.P. Stoicheff, Angular dependence of maser-stimulated Raman radiation in calcite. Phys. Rev. Lett. **12**, 290–293 (1964)
5. A.Z. Grasiuk, L.L. Losev, A.P. Lutsenko, S.N. Sazonov, Parametric Raman anti-Stokes laser. Sov. J. Quantum Electron. **20**(10), 1153–1155 (1990)
6. R.P. Mildren, D.W. Coutts, D.J. Spence, All-solid-state parametric Raman anti-Stokes laser at 508 nm. Opt. Express **17**, 810–818 (2009)
7. C. Wang, X. Zhang, Q. Wang, Zh Cong, Zh Liu, W. Wei, W. Wang, Zh Wu, Yu. Zhang, L. Li, X. Chen, P. Li, H. Zhang, Sh Ding, Extracavity pumped $BaWO_4$ anti-Stokes Raman laser. Opt. Express **21**, 26014–26026 (2013)
8. J.A. Giordmaine, W. Kaiser, Light scattering by coherently driven lattice vibrations. Phys. Rev. **144**, 676–690 (1966)
9. S.N. Smetanin, A.V. Fedin, A.S. Shurygin, Realisation of four-wave mixing phase matching for frequency components at intracavity stimulated Raman scattering in a calcite crystal. Quantum Electron. **43**, 512–518 (2013)

10. S.N. Smetanin, M. Jelinek, V. Kubecek, H. Jelinkova, A.S. Shurygin, Four-wave-mixing and nonlinear cavity dumping of 280 picosecond 2nd Stokes pulse at 1.3 μm from Nd:SrMoO$_4$ self-Raman laser. Laser Phys. Lett. **13**, 015801 (2016)

11. S.N. Smetanin, M. Jelinek, V. Kubecek, H. Jelinkova, Low-threshold collinear parametric Raman comb generation in calcite under 532 and 1064 nm picosecond laser pumping. Laser Phys. Lett. **12**, 095403 (2015)

12. M.C. Pujol, M. Rico, C. Zaldo, R. Sol, V. Nikolov, X. Solans, M. Aguil, F. Daz, Crystalline structure and optical spectroscopy of Er^{3+}-doped KGd(WO$_4$)$_2$ single crystals. Appl. Phys. B **68**, 187–197 (1999)

13. J. Warner, Phase-matching for optical up-conversion with maximum angular aperture—theory and practice. Opto-Electronics **1**, 25–28 (1969)

14. N.P. Barnes, J. Corcoran, Parametric generation processes: special bandwidth and acceptance angles. Appl. Opt. **15**, 696–699 (1976)

15. M.J.T. Milton, T.J. McIlveen, D.C. Hanna, P.T. Woods, High-efficiency infrared generation by difference-frequency mixing using tangential phase matching. Opt. Comm. **87**, 273–277 (1992)

16. V.G. Dmitriev, G.G. Gurzadyan, D.N. Nikogosyan, *Handbook of Nonlinear Optical Crystals* (Springer, Berlin, 1999)

17. Handbook of Optics. Volume IV: Optical Properties of Materials, Nonlinear Optics, Quantum Optics. Third Edition / Ed. by M. Bass (New York: The McGraw-Hill Companies, Inc., 2010)

18. S.N. Smetanin, M.E. Doroshenko, L.I. Ivleva, M. Jelinek, V. Kubecek, H. Jelinkova, Low-threshold parametric Raman generation of high-order Raman components in crystals. Appl. Phys. B **117**, 225–234 (2014)

19. S.A. Akhmanov, N.I. Koroteev, Spectroscopy of light scattering and nonlinear optics. Nonlinear-optical methods of active spectroscopy of Raman and Rayleigh scattering. Sov. Phys. Usp. **20**(11), 899–936 (1977)

20. S.S. Sementsov, L.D. Khazov, Anisotropy of the stimulated Raman scattering in Iceland spar. Sov. J. Quantum Electron. **5**(1), 114–114 (1975)